

29 **Key Points:**

- 30 • An empirical model using three tropical forcings accurately describes 50–80% of peak
31 monsoon precipitation variability in Southern Africa.
- 32 • Significant prediction skill exists with up to five months lead time, which is weakest
33 when the identified forcings are highly correlated
- 34
- 35 • Seasonal forecast systems underperform the empirical model as they skillfully represent
36 the forcings but lack accuracy in teleconnections.

37 **Abstract**

38 Rainfed agriculture is the mainstay of economies across Southern Africa (SA), where most
39 precipitation is received during the austral summer monsoon. Despite that, seasonal precipitation
40 predictability in SA is less explored. Here we use three natural climate forcings, El Niño–
41 Southern Oscillation (ENSO), Indian Ocean Dipole (IOD), and the Indian Ocean Precipitation
42 Dipole (IOPD) – the dominant precipitation variability mode – to construct an empirical model
43 that exhibits significant skill over SA during monsoon in explaining precipitation variability and
44 in forecasting it with a five-month lead. While most explained precipitation variance (50–75%)
45 comes from contemporaneous IOD and IOPD, preconditioning all three forcings is key in
46 predicting monsoon precipitation with a zero to five-month lead. Seasonal forecasting systems
47 accurately represent the interplay of the three forcings but show varying skills in representing
48 their teleconnection over SA. This makes them less effective at predicting monsoon precipitation
49 than the empirical model.

50 **Plain Language Summary**

51 Accurately predicting precipitation is crucial for agricultural planning in Southern Africa (SA),
52 as the region is prone to droughts and floods. Here we develop an empirical model employing
53 sea surface temperature and precipitation indexes from the Pacific and Indian Oceans to forecast
54 average precipitation in SA from December through February. It can account for approximately
55 half of the variation in Southern African precipitation with a five-month lead time and about
56 three-fourths of the variation using December preconditions. The empirical model outperforms
57 seasonal forecast systems when considering the same lead times. Although seasonal forecast
58 systems can skillfully predict modes of variability related to sea surface temperatures and
59 precipitation in the two oceanic basins, they are less consistent in predicting the relationship
60 between their indexes and precipitation over Southern Africa. Specifically, they show a stronger
61 correlation between Pacific Ocean temperatures and Southern African precipitation and too weak
62 correlation with the Indian Ocean.

63 **1 Introduction**

64 Southern Africa (SA) is a drought- and flood-prone region of the world where over 95%
65 of agriculture relies on seasonal precipitation primarily occurring during the austral summer
66 monsoon (Ashfaq et al., 2020; Mpungose et al., 2022; Reason & Rouault, 2002; Wetterhall et al.,
67 2014; Winsemius et al., 2014). Most of the precipitation during the peak of the monsoon season
68 (December to February) is enhanced by tropical lows and, in some cases, tropical cyclones that
69 form within the tropics and move westward over Africa (Barimalala et al., 2020; Howard et al.,
70 2019; Ibebuchi, 2023a).

71 Earlier studies suggested that El Niño–Southern Oscillation (ENSO) and Indian Ocean
72 Dipole (IOD) are the two primary mechanisms contributing to SA monsoon seasonal variability
73 (Crétat et al., 2019; Howard et al., 2019; Ibebuchi, 2023b; Manatsa et al., 2012; Reason &
74 Jagadheesha, 2005), while Madden Julian Oscillation (MJO) is responsible for intraseasonal
75 variability (De Andrade et al., 2021; Silvério & Grimm, 2022). Beyond providing
76 contemporaneous forcing, the IOD has also been shown to predict austral summer precipitation
77 with several months lead (Ibebuchi, 2023b). However, IOD and ENSO are usually not
78 independent of each other. Therefore, it is only possible to independently attribute precipitation

79 variability to one with accounting for the other's influence. Recent studies also suggest that the
80 leading mode of precipitation variability in the Indian Ocean (IO) mediates tropical forcings
81 effects in distant regions (Abid et al., 2020, 2023; Horan et al., 2023; Mehmood et al., 2022).
82 However, it is currently unknown whether it plays a role in mediating ENSO and IOD influences
83 over SA during monsoon or has a distinct role that can be leveraged to predict monsoon
84 precipitation.

85 Accurate seasonal predictability of monsoon precipitation across SA can be a key to
86 sustainable agricultural practices. Evidence of seasonal precipitation predictability over parts of
87 SA relates to Pacific and Indian oceans Sea Surface temperature (SST) variability (De Andrade
88 et al., 2021; Ibebuchi, 2023b; Landman et al., 2012; Monerie et al., 2019; Reason et al., 2006).
89 However, neither the sources of predictability nor empirical and dynamical models have been
90 fully exploited for predicting monsoon precipitation in SA (Landman et al., 2012; Landman &
91 Beraki, 2012; Munday & Washington, 2017). To further our understanding of the SA monsoon,
92 we develop an empirical model using ENSO, IOD, and the dominant precipitation mode in the
93 IO as leading precursors and contemporaneous forcings. This model examines the roles of these
94 factors in precipitation variability and predictability across SA. In addition, we analyze the
95 skillfulness of two seasonal forecasting systems, the Geophysical Fluid Dynamics Laboratory
96 (GFDL) Seamless System for Prediction and Earth System Research (SPEAR; Delworth et al.,
97 2020) and the European Center for Medium-Range Weather Forecasts (ECMWF) fifth-
98 generation seasonal forecasting system (SEAS5; Johnson et al., 2019), in predicting monsoon
99 over SA with initializations at zero-, two-, and five-months lead. We aim to answer two key
100 questions using this analytical framework: 1) What are the roles of ENSO, IOD, and the
101 dominant IO precipitation mode in monsoon precipitation variability and predictability over SA?
102 How effective are SPEAR and SEAS5 in predicting summer monsoon over SA, and can their
103 skillfulness or lack thereof be explained by their capability or shortcoming to represent the
104 influences of these three natural forcings?

105 **2 Data and Methods**

106 This study uses precipitation and atmospheric variables from ECMWF's Fifth Generation
107 Reanalysis (ERA5; Hersbach et al., 2020) for data consistency required in teleconnection
108 analyses (Mukherjee et al., 2020). We analyze monthly precipitation, SST, and three-
109 dimensional atmospheric winds, divergence, and vertical pressure velocity. ERA5 precipitation
110 compares reasonably with the Climate Research Unit (CRU) Timeseries 4.07. (Harris et al.,
111 2020). However, a substantial disparity exists between CRU and Climate Prediction Center
112 (CPC; Xie et al., 2007) over SA (Figure S1), with CPC being substantially drier.

113 Moreover, two seasonal forecasting systems are analyzed for their skillfulness in
114 predicting the SA monsoon: GFDL's SPEAR with 15 members and ECMWF's SEAS5 with 25
115 members. We use zero-, two-, and five-month lead simulations, initialized in December,
116 October, and July for SPEAR, while SEAS5 only has data for zero- and two-month
117 lead simulations, initialized in December and October. The analysis period covers 1991 through
118 2022, which overlaps in all three datasets (ERA5, SEAS5, and SPEAR). All data is linearly
119 detrended before use except for climatological analyses.

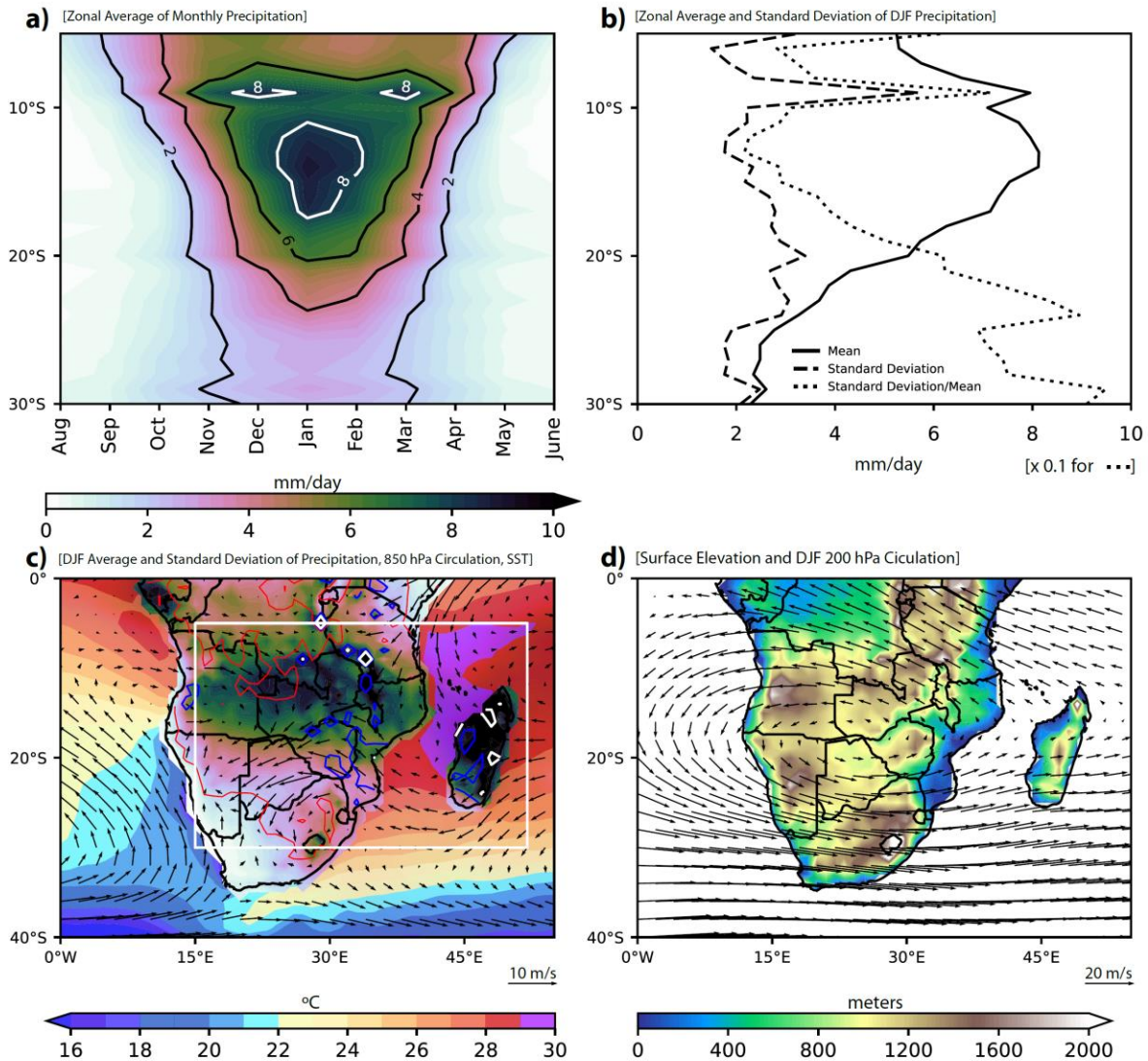
120 The analyses cover land areas south of 5°S for the austral summer months (December to
121 February; DJF). While the rainy season substantially varies latitudinally across SA, DJF is the
122 region's core monsoon season (Ashfaq et al., 2020). We investigate monsoon
123 precipitation variability and predictability using three natural modes of variability: ENSO, IOD,
124 and the dominant mode of precipitation variability in the IO, hereafter termed the IO
125 Precipitation Dipole (IOPD; Horan et al., 2023). We define the ENSO index as the Principal
126 Component (PC) of the first Empirical Orthogonal Function (EOF) of monthly SSTs in the
127 Pacific covering 160°W–80°E and 10°S–10°N (Figure S2). The PC-based ENSO index strongly
128 correlates with SST-based Niño indexes. It is preferred over choosing one of the four Niño
129 indexes to minimize issues related to ENSO diversity. The IOD (Saji et al., 1999) is defined
130 using the standardized difference in SSTs between the Western (50°E–70°E, 10°S–10°N)
131 and Eastern (90°E–110°E, 10°S–0°) IO. Some studies have used the Subtropical IOD (SIOD)
132 index to investigate SA's precipitation variability (Behera & Yamagata, 2001; Hoell et al., 2017;
133 Ibebuchi, 2023a; Reason, 2001). Our analyses didn't find it more relevant than IOD (not shown).
134 IOPD is the PC of the first EOF of monthly precipitation in the IO, covering 40°E–140°E and
135 10°S–10°N (Figure S1; Horan et al., 2023).

136 We use multiple linear regression (MLR), simple Pearson correlation, and partial
137 correlation analyses to investigate the individual and combined influences of three modes
138 of variability on SA monsoon precipitation. A two-tailed T-test determines the significance of
139 regression coefficients, while an F-test determines the added value of each independent variable
140 in the MLR model. All results are tested for significance at 95% confidence. The MLR model is
141 further tested for overfitting by comparing the coefficient of determination (R^2) and predicted R^2 .
142 For calculating predicted R^2 , we remove each data point from the time series at each grid point,
143 calculate the regression equation, and subsequently use that equation to predict the removed data
144 point. The process is repeated for each data point until we have a time series that is completely
145 predicted based on the regression model.

146 **3 Results and Discussion**

147 The rainy season in SA varies significantly with latitude, from three months south of
148 20°S to over six months at 10°S (Figure 1a). The seasonal march of monsoon rains over SA
149 starts in November (Figures 1a, S1, S3), the onset month (Ashfaq et al., 2020). DJF is the core
150 monsoon season as zonal average precipitation exceeds 2 mm/day throughout the latitudinal belt
151 between 5°S and 30°S. Monsoon withdraws from most of the region in March (Figure S3;
152 Ashfaq et al., 2020). The seasonal maximum of average precipitation and its variability occurs at
153 the boundary of the dryline or Congo air boundary (Figure 1b, 1c; Howard & Washington,
154 2019). A comparable seasonal precipitation distribution with a low interannual variability is also
155 observed between northern Mozambique and Angola. South of that, precipitation exhibits a
156 latitudinally expanding east-west

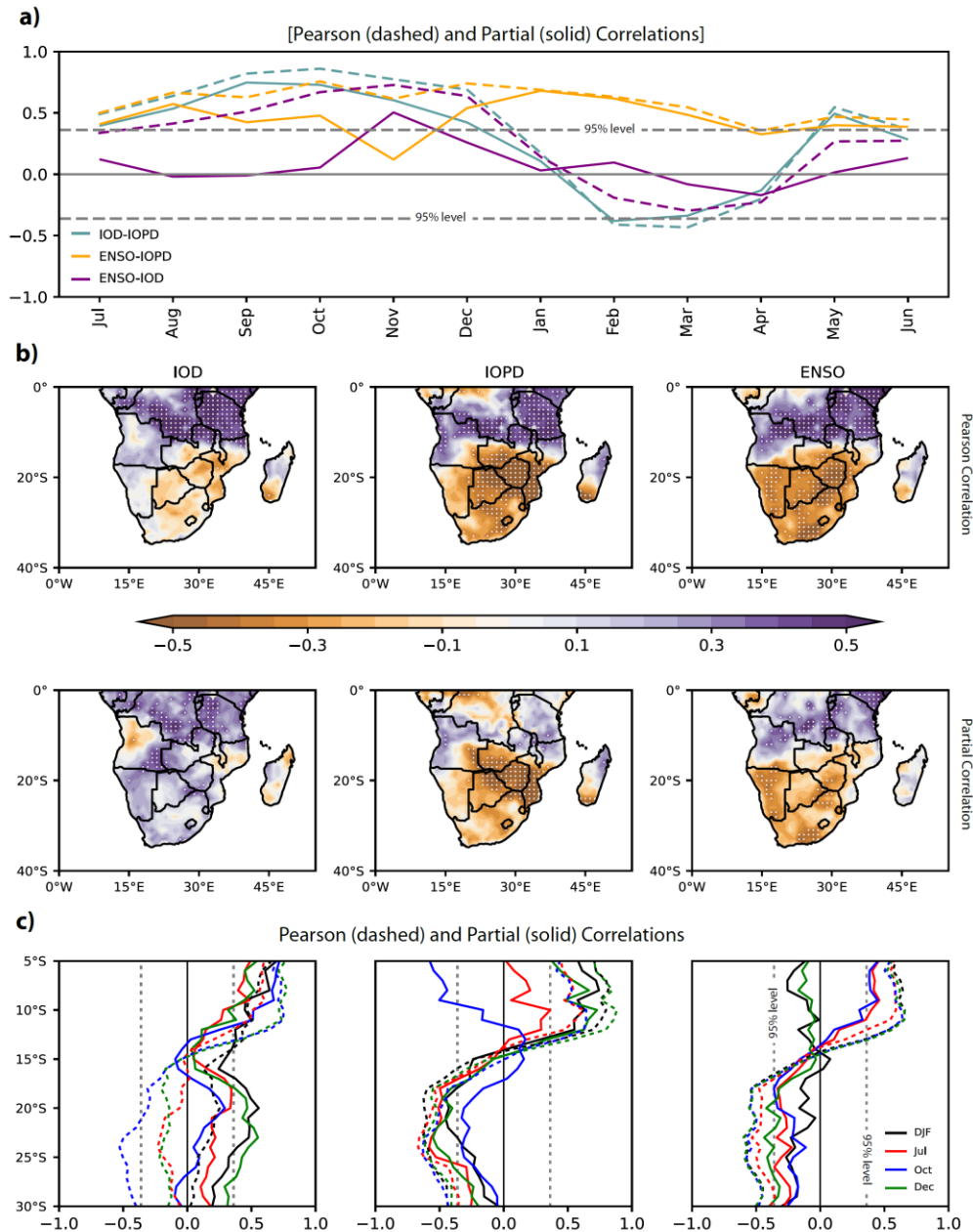
157



158

159 **Figure 1. Zonally averaged (5°E–52°E, land points) monthly precipitation (a), DJF mean,**
 160 **and standard deviation of precipitation, along with the ratio of standard deviation to the**
 161 **mean (b). c) Color contours: DJF surface temperature (ocean) and precipitation (land), line**
 162 **contours: DJF precipitation standard deviation (red, blue, white: 1, 2, 3 mm/day), vectors:**
 163 **winds at 850 hPa. The white box indicates the core study area. d) 200 hPa winds and**
 164 **topography over Southern Africa. Analyses cover 1991–2022 in ERA5.**

165 gradient with higher magnitudes east of the Kalahari Desert and little precipitation in its west.
 166 The proportion of precipitation variability relative to the mean increases over regions south of
 167 15°S (Figure 1b). The north-south precipitation gradient also extends from mainland Africa to
 168 Madagascar. SA receives the most moisture from continental recycling, while the warm IO
 169 (Figure 1c) contributes the major oceanic moisture source to continental precipitation (Geppert et
 170 al., 2022). Several key dynamical features regulate the spatially complex distribution of monsoon
 171 precipitation over SA. In the lower atmosphere (850 hPa), these features include the Angolan
 172 Low



173

174 **Figure 2. a) The monthly Pearson (dashed) and partial (solid) correlation between ENSO,**
 175 **IOD, and IOPD. b) DJF Pearson (second row) and partial (third row) correlations between**
 176 **precipitation over Southern Africa and IOD (left), IOPD (center), and ENSO (right). c)**
 177 **Zonal average of Pearson (dashed) and partial (solid) correlations of DJF precipitation**
 178 **(5°E–52°E, land points) with DJF, December, October, and July indexes of IOD, IOPD,**
 179 **and ENSO. Stippling in (b) and vertical dashed lines in (c) represent statistical significance**
 180 **($p < .05$).**

181

182 (AL) in the northwest, the Mozambique Channel Trough (MCT) between central Mozambique
183 and Madagascar, and the diagonally oriented South Indian Convergence Zone (SICZ) off the
184 southeast coast of SA (Figure 1c). The upper atmosphere circulations (200 hPa; Figure 1d) are
185 characterized by a high extending between the South Atlantic and Indian oceans with an
186 approximate center at the border of Zambia, Botswana, and Zimbabwe, commonly called the
187 Botswana High (BH). The role of these dynamical features in maintaining the summer monsoon
188 over SA has been described extensively in several earlier studies (Barimalala et al., 2020; Cook,
189 2000; Crétat et al., 2019; Driver & Reason, 2017).

190 Several studies have investigated how prevailing ENSO and IOD forcing or their
191 preconditioning shape precipitation distribution in SA (Crétat et al., 2019; Gore et al., 2020;
192 Howard et al., 2019; Ibebuchi, 2023b; Manatsa et al., 2012; Reason & Jagadheesha, 2005;
193 Reason & Rouault, 2002); however, despite its proximity, IOPD's role is currently unknown. The
194 three modes exhibit varying contemporaneous correlations throughout the year (Figure 2a). The
195 strongest and most consistent is the relationship between ENSO and IOPD, which peaks in
196 boreal winter. ENSO also correlates with IOD in the latter half of the year, but this correlation is
197 mostly insignificant after accounting for the effect of IOPD on their relationship, indicating that
198 IOPD acts as a mechanism for physically connecting SST variability in the Pacific and Indian
199 oceans. The relationship between IOD and IOPD is strongest during the fall season.

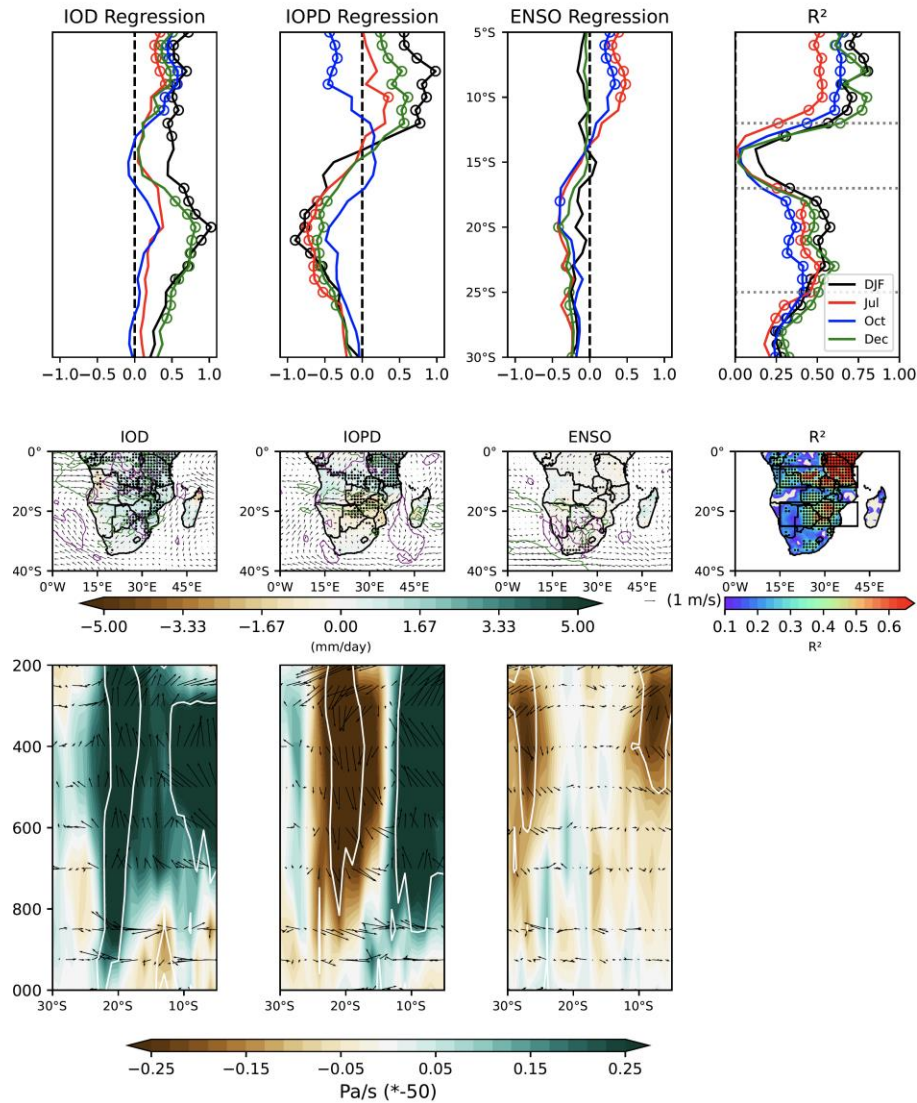
200 The contemporaneous simple Pearson correlations of the three modes with monsoon
201 precipitation over SA suggest a similar dipolar influence by ENSO and IOPD,
202 transitioning between negative in the south and positive in the north around 15°S (Figure 2b).
203 Most of the IOD's influence is positive but statistically significant only in areas north of
204 Mozambique. The similarity between ENSO and IOPD is remarkable but not surprising. In a
205 recent study, it was determined that ENSO's influence on boreal winter precipitation variability
206 over some regions is primarily driven by atmospheric diabatic heating anomalies caused by
207 ENSO-driven precipitation variability in the IO because of the strong coupling between IOPD
208 and ENSO at a seasonal scale (Abid et al., 2023; Horan et al., 2023). This is also true in SA,
209 where the direct influence of contemporaneous ENSO forcing on monsoon precipitation
210 becomes insignificant after controlling for the effects of IOPD and IOD (Figure 2b). IOD, in
211 contrast, becomes a significant positive forcing over SA after controlling for ENSO and IOPD,
212 while IOPD's influence remains mostly unchanged over SA's eastern half, north of SICZ, after
213 controlling for ENSO and IOD.

214 Our analysis shows that predicting monsoon precipitation in SA with significant skill is
215 possible using ENSO, IOD, and IOPD precursors. We demonstrate this by examining the
216 preconditioning of these natural modes in December, October, and July as predictors of the
217 summer (DJF) monsoon in SA. First, we examine their lead simple Pearson and partial
218 correlations with SA's monsoon precipitation to explain their predictive power (Figure 2c, S4).
219 The strength of correlations among the three modes varies during these months (Figure 2a),
220 resulting in different contributions to SA's precipitation predictability. In July, correlations
221 between the three natural modes are weaker, which means each mode can have a more distinct
222 and independent role in predicting monsoon precipitation. ENSO and IOPD lead correlations
223 retain dipolar patterns like their contemporaneous correlations (Figure 2c, dotted red). However,
224 unlike ENSO's limited contemporaneous role, controlling for IOD and IOPD retains most of

225 its lead correlation, except for southeast SA, north of SICZ, where lead IOPD forcing has a more
226 significant negative impact (Figure 2c, solid red). The July IOD shows precipitation
227 controls like those in its contemporaneous relationship with the SA monsoon. In October, the
228 strongest IOPD-IOD coupling is observed (Figure 2a). As a result, the October IOD exhibits a
229 dipolar correlation with precipitation, like ENSO and IOPD (Figure 2c; dotted blue, Figure S4).
230 After controlling for the other two factors, the IOPD correlation becomes mostly negative, while
231 the IOD correlation becomes positive. ENSO retains a dipolar influence pattern. In December,
232 dipolar patterns persist, although IOD's negative influence is relatively insignificant (Figure S4).
233 ENSO (IOD) partial correlations with the precipitation are mostly negative (positive), while the
234 IOPD relationship remains dipolar (Figure 2c; solid green). These analyses suggest that all three
235 forcings play a role in monsoon variability in SA, and their interplay helps determine its
236 predictability.

237 Next, we construct an MLR model using ENSO, IOD, and IOPD as independent
238 variables or predictors and gridded precipitation over SA as the dependent variable to examine
239 the extent to which precipitation variability can be explained through their
240 contemporary forcings or preconditioning. Given the latitudinal contrast in their influences, the
241 results are presented spatially (Figure S5) and in zonal averages (Figure 3). Several key points
242 from this analysis can be summarized: 1) The strong coupling between ENSO and IOPD in DJF
243 eliminates the independent role of contemporary ENSO forcing on monsoon precipitation
244 beyond what is already propagated by IOPD (Figure 3b; black). As for the ENSO
245 preconditioning, its predictive power is also the weakest, with statistically significant influence
246 limited to SA's northernmost and southernmost parts (Figure 3c; black, Figure S5). 2) The IOD
247 influence is predominantly positive and significant across all latitudes in DJF and with
248 December preconditioning. However, its most robust influence is limited to
249 the northernmost parts, with July and October preconditioning (Figure 3a; blue and red). The
250 IOPD is the most prominent force, exerting strong dipolar influence in the north (positive; 5°S–
251 12°S) and south (negative; 17°S–25°S), except in October when strong coupling with IOD limits
252 its distinct role in predicting SA monsoon. Spatiotemporally varying roles of these natural
253 forcings suggest that they can counteract or amplify one another's effect.

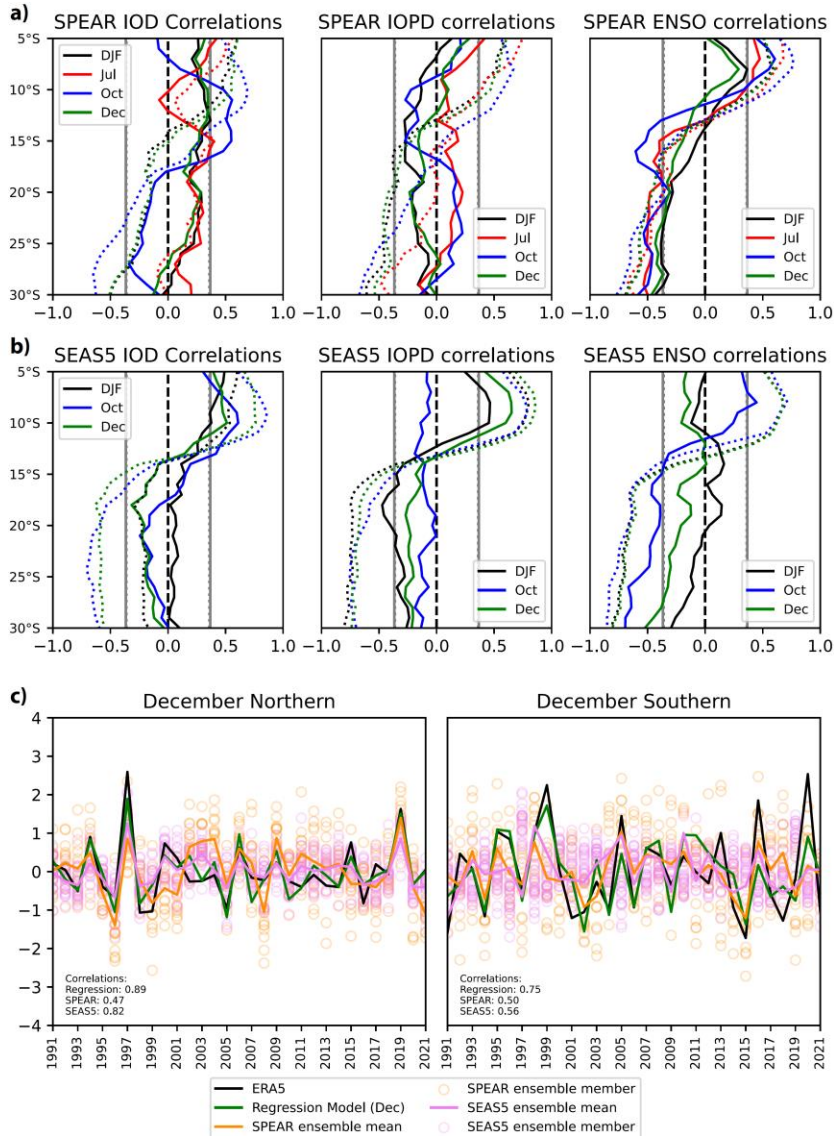
254



255

256 **Figure 3. Zonally averaged partial regression coefficients of contemporaneous and lead**
 257 **(December, October, and July) IOD (a), IOPD (b), and ENSO (c) forcings in DJF**
 258 **precipitation multi-linear regression (MLR) models. Circles indicate statistical significance.**
 259 **d) The R^2 for MLR models in (a-c). (e-g) Same as in (a-c; black) but shown spatially for**
 260 **contemporaneous forcings-based MLR for DJF precipitation (colors) and 850 hPa winds**
 261 **(vectors). Green (purple) contours represent the statistical significance of the zonal**
 262 **(meridional) winds regression coefficient. h) The R^2 for the MLR model in (e-g). Black**
 263 **boxes indicated northern and southern regions. (i-k) Same as in (e-g) but for the zonally**
 264 **averaged vertical cross-section of DJF divergence (multiplied by $10E6$) and vertical**
 265 **pressure velocity (multiplied by -50), shown as vectors. The regression coefficients related**
 266 **to vertical pressure velocity are also shown in color. White contours represent the**
 267 **statistical significance of colored contours. Statistical significance is at $p < .05$.**

268



269

270 **Figure 4. Zonally averaged partial (solid) and Pearson (dotted) correlation between DJF**
 271 **precipitation (5°E–52°E, land points) and contemporaneous and lead indexes of IOD (left),**
 272 **IOPD (center), and ENSO (right) in (a) SPEAR and (b) SEAS5. The vertical lines represent**
 273 **statistical significance ($p < 0.05$).** c) The mean area-averaged precipitation over northern (
 274 **left) and southern (right) parts of Southern Africa (rectangles in Figure 3h) in ERA5**
 275 **(black), MLR model (green), SPEAR (orange) ensemble mean, and SEAS5 (violet)**
 276 **ensemble mean. The empirical (dynamical) models represent December forcings**
 277 **(initializations). Light circles indicate ensemble members in SPEAR and SEAS5.**

278

279 Overall, the empirical model explains ~50% to >75% (~35% to >50%) zonally averaged
280 precipitation variability in areas along the 5°S–12°S (17°S–25°S). Spatially, the skill is
281 notably higher in southern Kenya and Tanzania, certain parts of Zambia, and within the region
282 north of SICZ, encompassing parts of Mozambique, Zimbabwe, and Botswana (Figure S5).
283 However, between 12°S and 17°S, predictability is limited due to the fluctuation between
284 negative and positive influences and inherent low precipitation variability (Figures 1b, 3a).
285 Regions with low predictability skills include northern Mozambique, central Zambia, southern
286 Malawi, and southern Angola.

287 How do these natural modes of variability influence the monsoon circulation
288 that eventually impacts precipitation? We explain it by regressing three-dimensional divergence,
289 vertical pressure velocity, and 850 hPa winds onto ENSO, IOD, and IOPD indexes. In DJF, IOD
290 enhances the moist flow in the lower atmosphere from continental Africa and the warm IO
291 through the Mozambique Channel and strengthens the deep convective environment throughout
292 the region except over Angola, where lower-level subsidence induced by the IOD suppresses
293 convection (Figure 3b, 3c). Overall, these dynamic anomalies lead to widespread enhanced
294 precipitation. IOPD, on the other hand, weakens MCT and SICZ, limiting moist flow over
295 southeast Africa and reducing precipitation. In areas south (north) of 15°S, it suppresses
296 (intensifies) the deep convective monsoon environment, weakening the southward seasonal
297 march of moist continental air. ENSO's most significant influence is over South Africa, which
298 enhances dry air entrainment from the southern Atlantic Ocean and reduces precipitation. It
299 otherwise has limited influence on the background monsoonal environment. Accordingly, DJF
300 atmospheric responses to ENSO, IOD, and IOPD July and October preconditioning provide a
301 physical explanation of their leading relationships with precipitation over southern Africa, as
302 shown in Figures 2, 3, S5, and S7.

303 We will now examine two seasonal forecasting systems, SPEAR and SEAS5, for their
304 skillfulness in predicting monsoon precipitation over SA within the context of the three
305 identified forcings. We begin by analyzing correlations between the modes and note that
306 models' ensemble mean can represent their varying relationships. For instance, the IOD–IOPD
307 correlation is strongest in October (SEAS5=0.89; SPEAR=0.89), as seen in reanalyses (ERA5 =
308 0.86). Similarly, the ENSO–IOPD coupling increases in December (SEAS5=0.81;
309 SPEAR=0.74), consistent with reanalyses (ERA5 = 0.75). July's initialized SPEAR ensemble
310 mean also shows a relatively weak correspondence between the three modes. Note that SEAS5
311 does not provide forecast data for DJF with the July initialization. However, models exhibit
312 biases in representing the influence of these modes on SA monsoon variability. The biases are
313 particularly severe in SPEAR. Compared to SEAS5, it lacks skill in representing the dipolar
314 pattern of lead Pearson correlations of three indexes with DJF precipitation (Figures 4, S8, S9).
315 Additionally, SPEAR and SEAS5 exhibit an overly strong influence of ENSO on precipitation
316 variability across SA. They show no significant influence of IOPD over SA's southeast in partial
317 correlations after accounting for the effects of IOD and ENSO (Figures 4, S8, S9), which
318 contrasts with reanalyses (Figures 2, S4). Similarly, IOD's positive association over latitudes
319 south of 17°S is also missing in its partial correlations (Figures 2, 4). Both models show a
320 negative IOD relationship instead. On the other hand, ENSO's partial correlations are overly
321 strong in both cases. SPEAR also fails to accurately represent the IOD and IOPD lead influences
322 in July initialized simulations.

323 Given the modeling errors in representing IOD, IOPD, and ENSO teleconnection across
324 SA during monsoon, its predictability is lower in dynamical models than in the empirical model.
325 Because of the contrasting influences of the three modes along the latitude, we assess the
326 predictability of two seasonal forecasting systems by analyzing time series of area average
327 precipitation over two regions, one between 5°S and 12°S where influence is predominantly
328 positive and one between 17°S and 25°S where influence is predominantly negative (Figures 4c,
329 S10). The empirical model using ENSO, IOD, and IOPD as predictors separately for July,
330 October, and December can account for 52%, 64%, and 79% of precipitation variance in the
331 northern part. It can also explain 46%, 44%, and 58% of precipitation variance in the southern
332 part. Please note that the empirical model does not suffer from overfitting, as the predicted R^2
333 closely follows the actual R^2 in all instances (Figure S11). While, by definition, the predicted R^2
334 is always lower than the actual R^2 , a significant difference between the two could indicate an
335 overfitting issue in the MLR model.

336 Due to strong coupling with IOD, IOPD loses most of its independent influence over the
337 southern part with October preconditioning. This results in a lower predictability with the
338 October lead. SPEAR-explained precipitation variance is 26%, 38%, and 25% in the northern
339 part and 0%, 25%, and 23% in the southern part with July, October, and December
340 initializations. Similarly, SEAS5-explained precipitation variance is 56% and 69% in the
341 northern part and 46% and 34% in the southern part with October and December initializations.
342 The substantially lower skill in SPEAR compared to SEAS5 is due to its much lower skill in
343 representing the influences of IOD and IOPD over both areas and ENSO influence over the
344 southern parts (Figure 4).

345 **4 Summary**

346 We have constructed an empirical model using three natural climate variability modes
347 related to SST and precipitation variability in the Pacific and Indian oceans (ENSO, IOD, IOPD).
348 This model effectively explains precipitation variance across SA during the core monsoon
349 season. Furthermore, these natural modes can also be utilized to predict monsoon precipitation in
350 SA with a five-month lead time. The three modes exhibit varying coupling strengths
351 throughout the year. For instance, IOPD is strongly coupled with IOD in the fall and ENSO in
352 the winter. These interdependencies between the three modes influence their distinct roles in
353 shaping precipitation variability over SA. A major component of ENSO's contemporaneous
354 teleconnection with SA is indirectly through its coupling with IOPD in the IO. Direct ENSO
355 forcing does not contribute anything substantial beyond IOPD's teleconnection pattern. IOPD's
356 forcing is a major contributor to precipitation predictability with different lead times. Its weakest
357 predictive power is in October because of the strong coupling between IOD and IOPD, which
358 limits IOPD's distinct role.

359 The SEAS5 and SPEAR models provide accurate information on varying monthly
360 correlations between ENSO, IOD, and IOPD. They also capture ENSO and IOPD interannual
361 variability precisely. However, their ability to describe IOD's interannual variability is less
362 effective. Moreover, SPEAR shows a poor simulation of their teleconnections in SA, particularly
363 below 17°S. As a result, both models underperform compared to the empirical model, with
364 SPEAR being the least effective in SA's southeast. These findings highlight the importance of

365 accurately representing ENSO, IOD, and IOPD teleconnections to enhance predictability in
366 seasonal forecasting systems during the summer monsoon in SA.

367

368 **Acknowledgments**

369

370 This research used the OLCF resources, a DOE Office of Science User Facility supported under
371 Contract DE-AC05-00OR22725. This work is supported by the U.S. Air Force Numerical
372 Weather Modeling Program and NCCR Center, located within the NNCCS at the ORNL and
373 supported under a Strategic Partnership Project 2316T849-08 between DOE and NOAA.

374

375 **Author contributions:**

376 M.F.H. and M.A. designed the study. M.F.H. performed the analyses. All authors were involved
377 in the discussion of results. M.A. and M.F.H. wrote the manuscript draft and finalized it with
378 feedback from all authors.

379

380 **Competing interests:**

381 The authors declare that they have no competing interests.

382

383 **Data and materials availability:**

384 All datasets used in this analysis are publicly available. The ERA5 reanalysis and SEAS5 model
385 data are available from the Copernicus Climate Change Service (C3S) Climate Data Store
386 (<https://cds.climate.copernicus.eu/>). SPEAR data is available from the North American Multi-
387 model Ensemble archive
388 (<http://iridl.ldeo.columbia.edu/SOURCES/.Models/.NMME/.GFDL-SPEAR/>). CPC Data is
389 available from NOAA's Physical Sciences Laboratory

390 (<https://psl.noaa.gov/data/gridded/data.cpc.globalprecip.html>). CRU Data is available from the
391 climatic research unit (<https://crudata.uea.ac.uk/cru/data/hrg/>). The analysis codes will be
392 provided upon acceptance of the manuscript.

393

394

395

396

397

398

399

400

401 **References**

- 402 Abid, M. A., Ashfaq, M., Kucharski, F., Evans, K. J., & Almazroui, M. (2020). Tropical Indian
403 Ocean Mediates ENSO Influence Over Central Southwest Asia During the Wet Season.
404 *Geophysical Research Letters*, 47(18), e2020GL089308. <https://doi.org/10.1029/2020GL089308>
- 405 Abid, M. A., Kucharski, F., Molteni, F., & Almazroui, M. (2023). Predictability of Indian Ocean
406 precipitation and its North Atlantic teleconnections during early winter. *Npj Climate and*
407 *Atmospheric Science*, 6(1), 17. <https://doi.org/10.1038/s41612-023-00328-z>
- 408 De Andrade, F. M., Young, M. P., Macleod, D., Hirons, L. C., Woolnough, S. J., & Black, E.
409 (2021). Subseasonal Precipitation Prediction for Africa: Forecast Evaluation and Sources of
410 Predictability. *Weather and Forecasting*, 36(1), 265–284. <https://doi.org/10.1175/WAF-D-20->
411 0054.1
- 412 Ashfaq, M., Cavazos, T., Reboita, M. S., Torres-Alavez, J. A., Im, E. S., Olusegun, C. F., et al.
413 (2020). Robust late twenty-first century shift in the regional monsoons in RegCM-CORDEX
414 simulations. *Climate Dynamics* 2020 57:5, 57(5), 1463–1488. <https://doi.org/10.1007/S00382->
415 020-05306-2
- 416 Barimalala, R., Blamey, R. C., Desbiolles, F., & Reason, C. J. C. (2020). Variability in the
417 Mozambique Channel Trough and Impacts on Southeast African Rainfall. *Journal of Climate*,
418 33(2), 749–765. <https://doi.org/10.1175/JCLI-D-19-0267.1>
- 419 Behera, S. K., & Yamagata, T. (2001). Subtropical SST dipole events in the southern Indian
420 Ocean. *Geophysical Research Letters*, 28(2), 327–330. <https://doi.org/10.1029/2000GL011451>
- 421 Cook, K. H. (2000). The South Indian Convergence Zone and Interannual Rainfall Variability
422 over Southern Africa. *Journal of Climate*, 13(21), 3789–3804. <https://doi.org/10.1175/1520->
423 0442(2000)013

- 424 Crétat, J., Pohl, B., Dieppois, B., Berthou, S., & Pergaud, J. (2019). The Angola Low:
425 relationship with southern African rainfall and ENSO. *Climate Dynamics*, *52*(3–4), 1783–1803.
426 <https://doi.org/10.1007/s00382-018-4222-3>
- 427 Delworth, T. L., Cooke, W. F., Adcroft, A., Bushuk, M., Chen, J. H., Dunne, K. A., et al. (2020).
428 SPEAR: The Next Generation GFDL Modeling System for Seasonal to Multidecadal Prediction
429 and Projection. *Journal of Advances in Modeling Earth Systems*, *12*(3), e2019MS001895.
430 <https://doi.org/10.1029/2019MS001895>
- 431 Driver, P., & Reason, C. J. C. (2017). Variability in the Botswana High and its relationships with
432 rainfall and temperature characteristics over southern Africa. *International Journal of*
433 *Climatology*, *37*, 570–581. <https://doi.org/10.1002/JOC.5022>
- 434 Eade, R., Smith, D., Scaife, A., Wallace, E., Dunstone, N., Hermanson, L., & Robinson, N.
435 (2014). Do seasonal-to-decadal climate predictions underestimate the predictability of the real
436 world? *Geophysical Research Letters*, *41*(15), 5620–5628.
437 <https://doi.org/10.1002/2014GL061146>
- 438 Geppert, M., Hartmann, K., Kirchner, I., Pfahl, S., Struck, U., & Riedel, F. (2022). Precipitation
439 Over Southern Africa: Moisture Sources and Isotopic Composition. *Journal of Geophysical*
440 *Research: Atmospheres*, *127*(21), e2022JD037005. <https://doi.org/10.1029/2022JD037005>
- 441 Gore, M., Abiodun, B. J., & Kucharski, F. (2020). Understanding the influence of ENSO patterns
442 on drought over southern Africa using SPEEDY. *Climate Dynamics*, *54*(1–2), 307–327.
443 <https://doi.org/10.1007/S00382-019-05002-W/FIGURES/15>
- 444 Harris, I., Osborn, T. J., Jones, P., & Lister, D. (2020). Version 4 of the CRU TS monthly high-
445 resolution gridded multivariate climate dataset. *Scientific Data 2020 7:1*, *7*(1), 1–18.
446 <https://doi.org/10.1038/s41597-020-0453-3>

- 447 Hersbach, H., Bell, B., Berrisford, P., Hirahara, S., Horányi, A., Muñoz-Sabater, J., et al. (2020).
448 The ERA5 global reanalysis. *Quarterly Journal of the Royal Meteorological Society*, *146*(730),
449 1999–2049. <https://doi.org/10.1002/qj.3803>
- 450 Hoell, A., Funk, C., Zinke, J., & Harrison, L. (2017). Modulation of the Southern Africa
451 precipitation response to the El Niño Southern Oscillation by the subtropical Indian Ocean
452 Dipole. *Climate Dynamics*, *48*(7–8), 2529–2540. <https://doi.org/10.1007/s00382-016-3220-6>
- 453 Horan, M., Kucharski, F., Johnson, N., & Ashfaq, M. (2023). Winter precipitation predictability
454 in Central Southwest Asia and its representation in seasonal forecast systems.
455 <https://doi.org/10.21203/RS.3.RS-3079978/V1>
- 456 Howard, E., & Washington, R. (2019). Drylines in Southern Africa: Rediscovering the Congo
457 Air Boundary. *Journal of Climate*, *32*(23), 8223–8242. <https://doi.org/10.1175/JCLI-D-19->
458 0437.1
- 459 Howard, E., Washington, R., & Hodges, K. I. (2019). Tropical Lows in Southern Africa: Tracks,
460 Rainfall Contributions, and the Role of ENSO. *Journal of Geophysical Research: Atmospheres*,
461 *124*(21), 11009–11032. <https://doi.org/10.1029/2019JD030803>
- 462 Ibebuchi, C. C. (2023a). Circulation Patterns Linked to the Positive Sub-Tropical Indian Ocean
463 Dipole. *Advances in Atmospheric Sciences*, *40*(1), 110–128. <https://doi.org/10.1007/s00376-022->
464 2017-2
- 465 Ibebuchi, C. C. (2023b). Patterns of atmospheric circulation linking the positive tropical Indian
466 Ocean dipole and southern African rainfall during summer. *Journal of Earth System Science*,
467 *132*(1), 13. <https://doi.org/10.1007/s12040-022-02025-6>

- 468 Johnson, S. J., Stockdale, T. N., Ferranti, L., Balmaseda, M. A., Molteni, F., Magnusson, L., et
469 al. (2019). SEAS5: The new ECMWF seasonal forecast system. *Geoscientific Model*
470 *Development*, 12(3), 1087–1117. <https://doi.org/10.5194/GMD-12-1087-2019>
- 471 Landman, W. A., & Beraki, A. (2012). Multi-model forecast skill for mid-summer rainfall over
472 southern Africa. *International Journal of Climatology*, 32(2), 303–314.
473 <https://doi.org/10.1002/JOC.2273>
- 474 Landman, W. A., Dewitt, D., Lee, D. E., Beraki, A., & Lötter, D. (2012). Seasonal Rainfall
475 Prediction Skill over South Africa: One- versus Two-Tiered Forecasting Systems. *Weather and*
476 *Forecasting*, 27(2), 489–501. <https://doi.org/10.1175/WAF-D-11-00078.1>
- 477 Manatsa, D., Reason, C. J. C., & Mukwada, G. (2012). On the decoupling of the IODZM from
478 southern Africa Summer rainfall variability. *International Journal of Climatology*, 32(5), 727–
479 746. <https://doi.org/10.1002/joc.2306>
- 480 Mehmood, S., Ashfaq, M., Kapnick, S., Gosh, S., Abid, M. A., Kucharski, F., et al. (2022).
481 Dominant controls of cold-season precipitation variability over the high mountains of Asia. *Npj*
482 *Climate and Atmospheric Science 2022 5:1*, 5(1), 1–13. [https://doi.org/10.1038/s41612-022-](https://doi.org/10.1038/s41612-022-00282-2)
483 [00282-2](https://doi.org/10.1038/s41612-022-00282-2)
- 484 Monerie, P. A., Robson, J., Dong, B., Dieppois, B., Pohl, B., & Dunstone, N. (2019). Predicting
485 the seasonal evolution of southern African summer precipitation in the DePreSys3 prediction
486 system. *Climate Dynamics*, 52(11), 6491–6510. [https://doi.org/10.1007/S00382-018-4526-](https://doi.org/10.1007/S00382-018-4526-3)
487 [3/FIGURES/3](https://doi.org/10.1007/S00382-018-4526-3)
- 488 Mpungose, N., Thoithi, W., Blamey, R. C., & Reason, C. J. C. (2022). Extreme rainfall events in
489 southeastern Africa during the summer. *Theoretical and Applied Climatology*, 150(1–2), 185–
490 201. <https://doi.org/10.1007/s00704-022-04162-w>

- 491 Mukherjee, S., Ashfaq, M., & Mishra, A. K. (2020). Compound Drought and Heatwaves at a
492 Global Scale: The Role of Natural Climate Variability-Associated Synoptic Patterns and Land-
493 Surface Energy Budget Anomalies. *Journal of Geophysical Research: Atmospheres*, *125*(11),
494 e2019JD031943. <https://doi.org/10.1029/2019JD031943>
- 495 Munday, C., & Washington, R. (2017). Circulation controls on southern African precipitation in
496 coupled models: The role of the Angola Low. *Journal of Geophysical Research: Atmospheres*,
497 *122*(2), 861–877. <https://doi.org/10.1002/2016JD025736>
- 498 Osman, M., & Vera, C. S. (2017). Climate predictability and prediction skill on seasonal time
499 scales over South America from CHFP models. *Climate Dynamics*, *49*(7–8), 2365–2383.
500 <https://doi.org/10.1007/S00382-016-3444-5/FIGURES/14>
- 501 Reason, C. J. C. (2001). Subtropical Indian Ocean SST dipole events and southern African
502 rainfall. *Geophysical Research Letters*, *28*(11), 2225–2227.
503 <https://doi.org/10.1029/2000GL012735>
- 504 Reason, C. J. C., & Jagadheesha, D. (2005). A model investigation of recent ENSO impacts over
505 southern Africa. *Meteorology and Atmospheric Physics*, *89*(1–4), 181–205.
506 <https://doi.org/10.1007/S00703-005-0128-9/METRICS>
- 507 Reason, C. J. C., & Rouault, M. (2002). ENSO-like decadal variability and South African
508 rainfall. *Geophysical Research Letters*, *29*(13), 16–1. <https://doi.org/10.1029/2002GL014663>
- 509 Reason, C. J. C., Landman, W., & Tennant, W. (2006). Seasonal to Decadal Prediction of
510 Southern African Climate and Its Links with Variability of the Atlantic Ocean. *Bulletin of the*
511 *American Meteorological Society*, *87*(7), 941–956. <https://doi.org/10.1175/BAMS-87-7-941>
- 512 Saji, N. H., Goswami, B. N., Vinayachandran, P. N., & Yamagata, T. (1999). A dipole mode in
513 the tropical Indian ocean. *Nature*, *401*(6751), 360–363. <https://doi.org/10.1038/43854>

- 514 Scaife, A. A., Arribas, A., Blockley, E., Brookshaw, A., Clark, R. T., Dunstone, N., et al. (2014).
515 Skillful long-range prediction of European and North American winters. *Geophysical Research*
516 *Letters*, *41*(7), 2514–2519. <https://doi.org/10.1002/2014GL059637>
- 517 Silvério, K. C., & Grimm, A. M. (2022). Southern African monsoon: intraseasonal variability
518 and monsoon indices. *Climate Dynamics*, *58*(3–4), 1193–1220. [https://doi.org/10.1007/s00382-](https://doi.org/10.1007/s00382-021-05954-y)
519 [021-05954-y](https://doi.org/10.1007/s00382-021-05954-y)
- 520 Wetterhall, F., Winsemius, H. C., Dutra, E., Werner, M., & Pappenberger, F. (2014). Seasonal
521 predictions of agro-meteorological drought indicators Seasonal predictions of agro-
522 meteorological drought indicators for the Limpopo basin Seasonal predictions of agro-
523 meteorological drought indicators. *Hydrol. Earth Syst. Sci. Discuss*, *11*, 861–888.
524 <https://doi.org/10.5194/hessd-11-861-2014>
- 525 Winsemius, H. C., Dutra, E., Engelbrecht, F. A., Archer Van Garderen, E., Wetterhall, F.,
526 Pappenberger, F., & Werner, M. G. F. (2014). The potential value of seasonal forecasts in a
527 changing climate in southern Africa. *Hydrology and Earth System Sciences*, *18*(4), 1525–1538.
528 <https://doi.org/10.5194/HESS-18-1525-2014>
- 529 Xie, P., Yatagai, A., Chen, M., Hayasaka, T., Fukushima, Y., Liu, C., & Yang, S. (2007). A
530 Gauge-Based Analysis of Daily Precipitation over East Asia. *Journal of Hydrometeorology*, *8*(3),
531 607–626. <https://doi.org/10.1175/JHM583.1>

532

533